Power Transmission by Using Laser Beams

By

Chobei YAMABE,* Keiji NAKAMURA,* Hiroshi HOMMA,** Masao YAMAUCHI,***
Tatsuo OKAMOTO,* Hiroyuki ISHIHARA,† Toshihiko NAKAMURA,††
Shigeyuki TAKAGI,††† and Kenji HORII*

(September 10, 1988)

Summary: A method of power transmission using a laser beam for a very long distance has been proposed. A compact and high power TEA CO_2 laser has been developed and it has been applied to the plasma production for the power transmission.

The characteristics of the direct energy conversion from laser energy to electricity with laser-produced plasma are reported here. It is found that the total conversion efficiency increases with laser output using a carbon target. The effect of surface magnetic confinement with geometric mirrors on the electric output power is also reported here.

1. INTRODUCTION

It has been proposed [*1*] to use a laser beam for energy transmission over an ultralong distance from a developing country which is rich in natural energy to a consuming city where there is need for large amounts of energy, or from a solar power satellite to the Earth or between space stations. On the other hand, power transmission by a microwave beam has been proposed by Glaser [*2*]. However, the demertis of a microwave beam are longer wavelength and therefore the necessity of very large equipment because of the large beam divergence and the low energy transmission density due to the air breakdown by the electric field of the microwave. Not many studies on the power transmission by using laser beams have been reported. The wavelength of laser light is much shorter than that of a microwave beam, and the electric field for the air breakdown with laser is higher compared with that [*3*] of the microwave, therefore, the transmission energy density can be increased. Since the conversion efficiency with a laser beam is inferior to that of a microwave beam, for which the method is supported by an established technique, it is important to improve the laser device in efficiency and output power at the region of wavelength which is called "the window of the atmosphere". It is also important to develop a high-efficiency direct energy converter from laser energy to electricity.

* Department of Electrical Engineering, Faculty of Engineering, Nagoya University
** Tohoku Electric Power Co.
*** Chubu Electric Power Co.
† Ishikawajima-Harima Heavy Industries Co., Ltd.
†† NGK Insulators, Ltd.
††† Toshiba Corporation

In this paper, characteristics of both an automatic preionized TEA CO_2 laser (λ = 10.6 μm) and the direct energy conversion from laser energy to electricity with laser-produced plasma are reported. The energy of the initially produced plasma by the TEA CO_2 laser is changed to the expansion energy with time, and the ion energy is converted effectively to the electricity by the electrostatic separation of the ions and electrons. A flowchart of the energy propagation for the power transmission by laser beams is shown in Fig. 1.

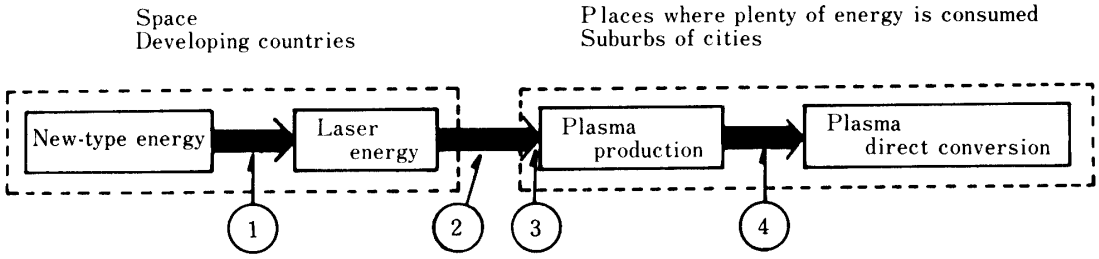

1. Conversion efficiency from electricity to laser beam
2. Laser propagation characteristic in the air
3. Laser interraction with produced plasma
4. Separation of ions from electrons
   Ion capture efficiency

Fig. 1. Flowchart of energy propagation.

2. Feature of Power Transmission Using Laser Beam

The divergent angle of θ of the laser beam due to the diffraction in the free space is given by $\theta \approx 1.22\ \lambda / D$ (rad). Where, D is the beam diameter at the output terminal and λ is the laser wavelength. The directivity for laser beam is improved with the order of $10^3 - 10^5$ which is the wavelength ratio of laser light to microwaves for the same beam diameter, so the receiver of laser beam will be compact compared with that of microwave. The relationship of the propagation distance L and the beam size D' at L for two different wavelengths (λ = 10.6 μm for CO_2 laser and λ = 1 cm for microwave) is shown in Table 1. In both cases, the beam diameter D is assumed to be 1 m. As the gas pressure decreases with the altitude, the breakdown electric field of the air E becomes a problem. The breakdown electric field of the air with pressure is shown in Fig. 2. The breakdown electric field of the air decreases with pressure and the value of E is about 1 kV/cm at 0.01 atm. On the contrary, in the case of laser method, the value of E does not change so much with pressure and is about 10 MV/cm.

The power density of transmission (Poynting's vector) P in the space of transmitted medium is calculated in Table 2 to compare the laser method with other various methods which have been practically used or will be used in near future. It is found from Table 2 that the power density with the laser beam is too large.

Table 1. Relationship between propagation distance and beam aperture as a function of wavelength.

Wavelength	D (m)	L (km)	$D'=D+L\cdot\theta$ (m)
10.6μm (CO_2 laser)	1	1	1
		100	2.3
		1,000	13.9
		10,000	130
1 (microwave)	1	1	13.2
		100	1221

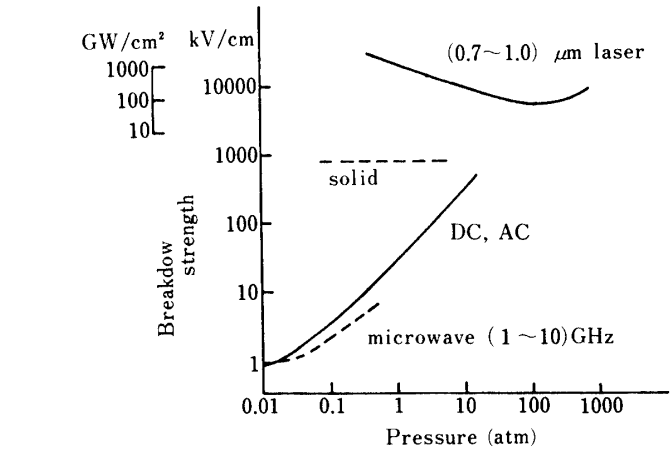

Fig. 2. Breakdown strength of air against pressure.

Table 2. Comparison of various methods for energy transmission.

Parameters / Methods	V_g (kV)	I (kA)	P_o (GW)	r (cm)	L (cm)	E_B (kV/cm)	B (KG)	E_a (kV/cm)	B_a (KG)	P (MW/cm^2)
Aerial cable	$500/\sqrt{3}$	1.2	1	1.7	1400	30	0.14	0.2	0.0013	0.00021
Oil-filled cable	$275/\sqrt{3}$	0.6	0.3	2.4	2.0	800-1000	0.05	80	0.035	2.2
Forced cooling pype-type Oil-filled cable	$500/\sqrt{3}$	1.8	1.5	2.8	3.0	1000	0.13	96	0.084	6.4
Compressed gas insulated cable (SF_6 6 atm)	$275/\sqrt{3}$	5.3	2.5	6.0	10.5	350	0.18	15	0.094	1.1
Union Carbide Co. AC super-conductive cable	$345/\sqrt{3}$	18	11	10	12	200	1	17	0.225	3.1
DC super-conductive cable estimation (Nb_3Sn)	–	–	–	–	–	200	100	24	32	614
Brookhaven National Lab. AC super-conductive cable (Nb_3Sn)	$138/\sqrt{3}$	4	1	2.5	1.4	140	0.33	57	0.25	11.4
DC super-conductive cable (Nb_3Sn)	$240/\sqrt{3}$	10	4.2	2.5	1.6	210-283	0.8	87	0.6	42
Laser beam	–	–	–	–	–	23000	76	800	2.7	1728

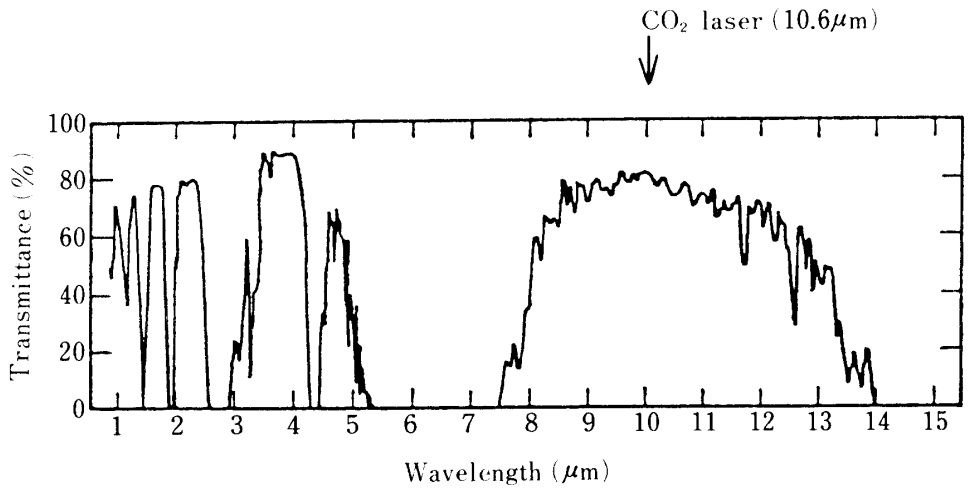

Fig. 3. Wavelength dependence of the transmittance of laser beam in the atmosphere.

According to the wavelength dependence of the transmittance of the laser beam in the atmosphere as shown in Fig. 3, there is a "window of the atmosphere" at some wavelength regions. For example, in case of CO_2 laser, some absorption by CO_2 molecules, etc., is observed [*4*] and the propagation loss in fine weather is about 20% for the propagation distance of 3600 km. Recently it has been proposed [*5*] to use the CO laser (λ = 5 μm) for energy transmission.

3. Development of a Compact and High Power Auto-Preionized tea CO_2 Laser for Plasma Production

3.1 Introduction

A TEA (Transversely Excited Atmospheric Pressure) CO_2 laser with a wavelength of 10.6 μm, in which molecules are excited by discharge, is popularly used and applied to many fields as optical and thermal sources. But even now there is a requirement to get more efficient, compact and high power laser device. So investigation from all approaches has been carried out, and it is suggested to operate at more than atmospheric pressure [*6*] - [*8*].

The transition from the glow discharge to the arc discharge occurs when the input energy density exceeds the critical value. Therefore, it is of importance to suppress the transition and to obtain the glow discharge. In order to suppress the glow-to-arc transition, the double discharge technique is often used in CO_2 laser and excimer laser. Then both the intensity and timing of preionization must be adjusted to the most suitable condition. In CO_2 laser, the delay time between the pre-discharge and the main discharge is controllable with the pressurized gap connected in series with the Marx bank [*9*] [*10*]. Another electrical circuit for preionization besides the main discharge circuit consited with the PFN (Pulse Forming Netowrk) is set up, and the delay time between the two electrical circuits can be controlled by two delay circuits in excimer laser [*11*]. Thus, although various ways for the preionization have been reported, in this paper, we describe another method to control the pre-discharge, and the characteristics of main discharge and laser output using this method are reported.

3.2 Experimental appratus and procedure

The electrical circuit is shown in Fig. 4. A cathod of 90 mm width and 700 mm length is made of aluminum and has ten parallel grooves on its surface [*12*] [*13*]. The cross-section of each groove is 4.5 mm and 3 mm deep. Many protrusions with the shape of trapezoid [*14*] are distributed along each groove to increase the threshold of glow-to-arc transition. A trigger electrode T covered with a pyrex glass tube is put each groove in along the laser axis. The outer diameter and thickness of the glass tube is 4 mm and 1.2 mm, respectively.

An anode with Chang profile [*15*] is the same size and material as the cathode. Main electrodes are separated by 30 mm and the active volume is about 0.45 l.

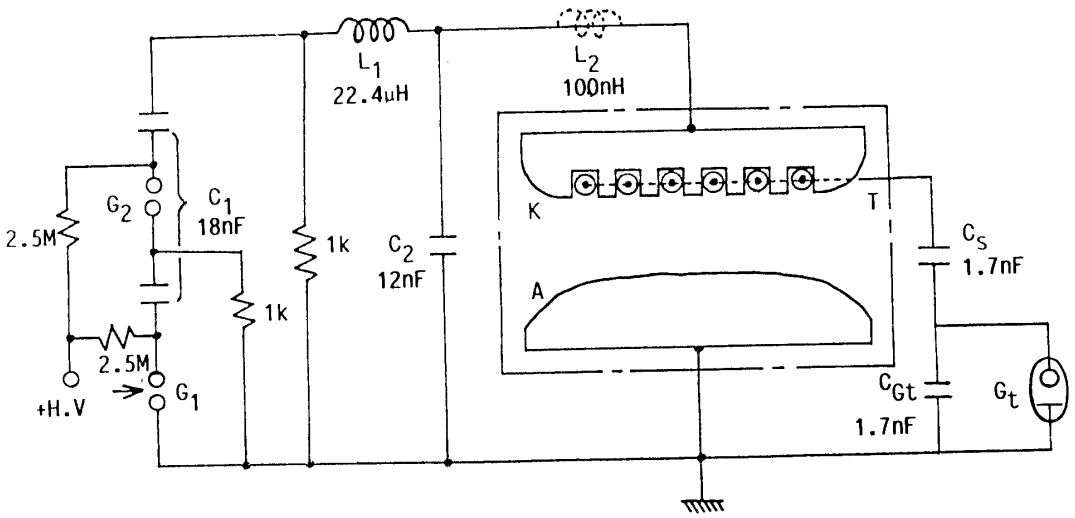

Fig. 4. Schematic diagram of experimental appratus and electrical circuit.

The electrical discharge circuit with PFN is composed of capacitance C_1, C_2, inductance L_1, L_2, and gap G_1, G_2 pressurized with nitrogen. The process of the discharge has been mentioned in detail in the reference 14. Before the main discharge, the voltage V between the anode and the cathode is given by the following equation.

$$V = V_1 C_1 (1 - \cos \omega t)/(C_1 + C_2) \tag{1}$$

where, $\omega = 1/(L_1 C)^{\frac{1}{2}}$

$$1/C = 1/C_1 + 1/[C_2 + (C_s C_g/(C_s + C_g))]$$
$$\fallingdotseq 1/C_1 + 1/C_2$$

V_1: applied voltage on the effective primary capacitor C_1
C_g: the capacitance of the glass tube

The trigger current passes through the TCC circuit in the following way. When V equal to about 3 kV, the corona discharge occurs between the cathode and the trigger electrode through the glass tube and then primary electrons are scattered on the surface of the cathode. At this time, the gap G_t does not operate yet, but when the voltage on the capacitance C_{Gt} increases with the voltage across the main electrodes, the gap G_t is automatically fired and the pulse current flows into the TCC circuit. The triggering time of the gap G_t is controlled by the gap separation of G_t. Here, amount of the electrical charge fed into the TCC circuit is divided into two parts as follows as shown in Fig. 5.

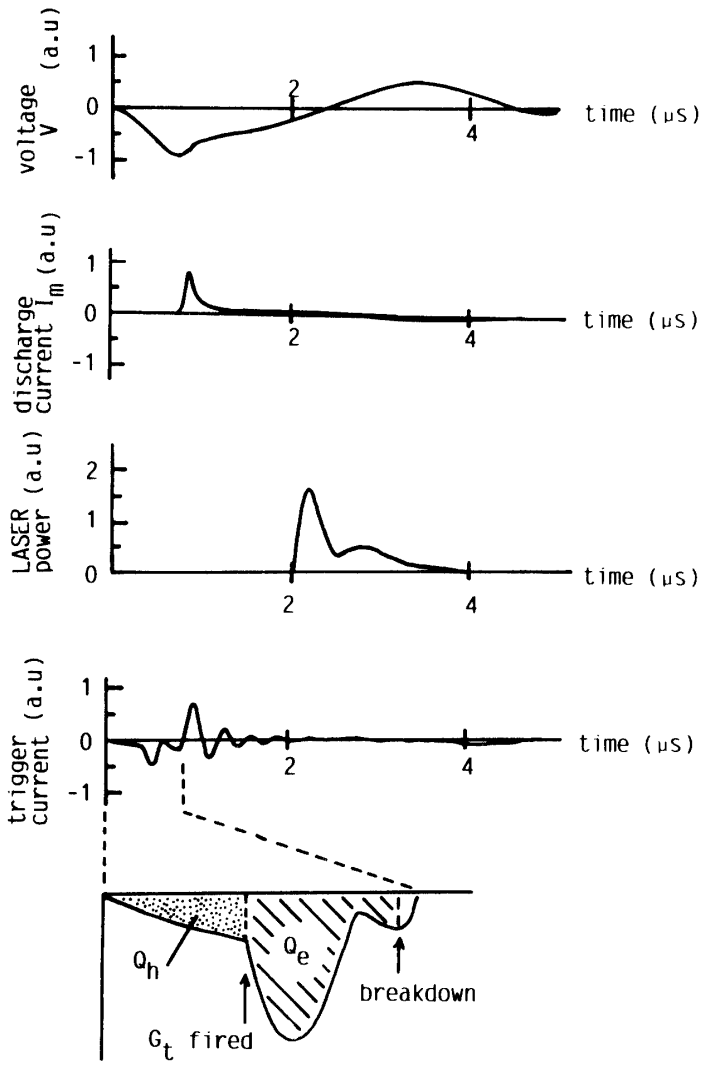

Fig. 5. Temporal characteristics of voltage across the main electrode, main discharge current, laser output power, trigger current. The definition of Q_h and Q_e is also shown in the lowest figure.

1) Q_h: amount of the electrical charge before the breakdown of the gap G_t
2) Q_e: amount of the electrical charge injected between the initiation of the breakdown of the gap G_t and the initiation of the main discharge
3) Q_t: amount of the electrical charge before the main discharge ($Q_t = Q_h + Q_e$)

Then, the value of Q_h depends on the capacitance C_s, C_{Gt}, and C_g, and the value of Q_t depends on the capacitance C_s and C_g. The laser device operating under the condition that the gap G_t is shortened is equivalent to the laser at which the corona discharge is used for the preionization as usual. We call "normal operation" in the case of operating under that condition (i.e. gap G_t is shortened).

A $CO_2/N_2/He$ mixture gas is flowed along the laser axis at atmospheric pressure. The optical resonator consists of a gold-coated reflector with a radius curvature of

10 m and a germanium flat coupler with a reflection of 51% and the length of resonator is about 2 m. The waveform of the laser output is detected using the reflection from a NaCl Brewster window by gold doped germanium detector cooled by liquid nitrogen. The waveforms of the voltage V and main discharge current I_m are measured by R-C divider and a search coil, respectively, and trigger current is measured by a Rogowski coil (Model-110: PEARSON ELECTRONICS, Inc.).

3.3 Experimental result and discussion

3.3.1 Effect on TCC circuit on main discharge

The voltage V, main discharge current I_m, trigger current I_t and laser power are shown in Fig. 5 at $t_{Gt\text{-}BD}$ = 300 ns. The $t_{Gt\text{-}BD}$ means the delay time between the breakdown of the gap G_t and the initiation of the main discharge. The operating parameters are V_1 = 35.6 kV, $CO_2/N_2/He$ = 1/1/5 (l/min), and $C_S = C_{Gt}$ = 1700 pF. The waveforms in both V and I_m before the glow-to-arc transition are independent of the delay time $t_{Gt\text{-}BD}$.

The spatial distribution and time-integrated photographs of radiation intensity along the glass tube are shown in Fig. 6 for parameters of $t_{Gt\text{-}BD}$ and the distance z from the cathode. As shown in Fig. 6, it is apparent that the more homogeneous glow discharge is obtained at $t_{Gt\text{-}BD}$ = 300 ns compared with normal operation at $t_{Gt\text{-}BD}$ = 750 ns. The reason is described later. The degree of uniformity of the main discharge varied with the delay time $t_{Gt\text{-}BD}$ even if there is no difference in the waveforms of both V and I_m.

3.3.2 Suppression of glow-to-arc transition and improvement of laser output by TCC circuit

As the input energy per unit discharge volume increases, the glow-to-arc transition tends to occur at one point on the electrodes, and the voltage between the anode and the cathode abruptly reduced. The suppression of the transition at the high input energy is important not only to obtain the high output energy, but also to prolong the life of laser device with the prevention against the erosion of electrodes and the deterioration of the laser gas. Here, we measured the characteristics of the main discharge and laser output for the intensity and the timing of the preionization.

In the case of $C_S = C_{Gt}$ = 1700 pF, $CO_2/N_2/He$ = 1/1/5 (l/min), the variations of the transition rate and the laser output as a function of $t_{Gt\text{-}BD}$ are shown in Fig. 7. At $t_{Gt\text{-}BD}$ = 300 ns, the transition rate is minimum and the laser output shows maximum value. So, it is evident that the control of the delay time $t_{Gt\text{-}BD}$ by the gap G_t is effective for suppression of the glow-to-arc transition. It is considered that laser output increased because the active volume became large to obtain the homogeneous glow discharge by suppression of glow-to-arc transition as shown in Fig. 6. The reason for the existence of the optimum of the delay time $t_{Gt\text{-}BD}$ for laser output is qualitatively as follows; If the delay time $t_{Gt\text{-}BD}$ is too long, the peak value of the trigger current is so small that few of primary electrons are produced and that a part of the primary

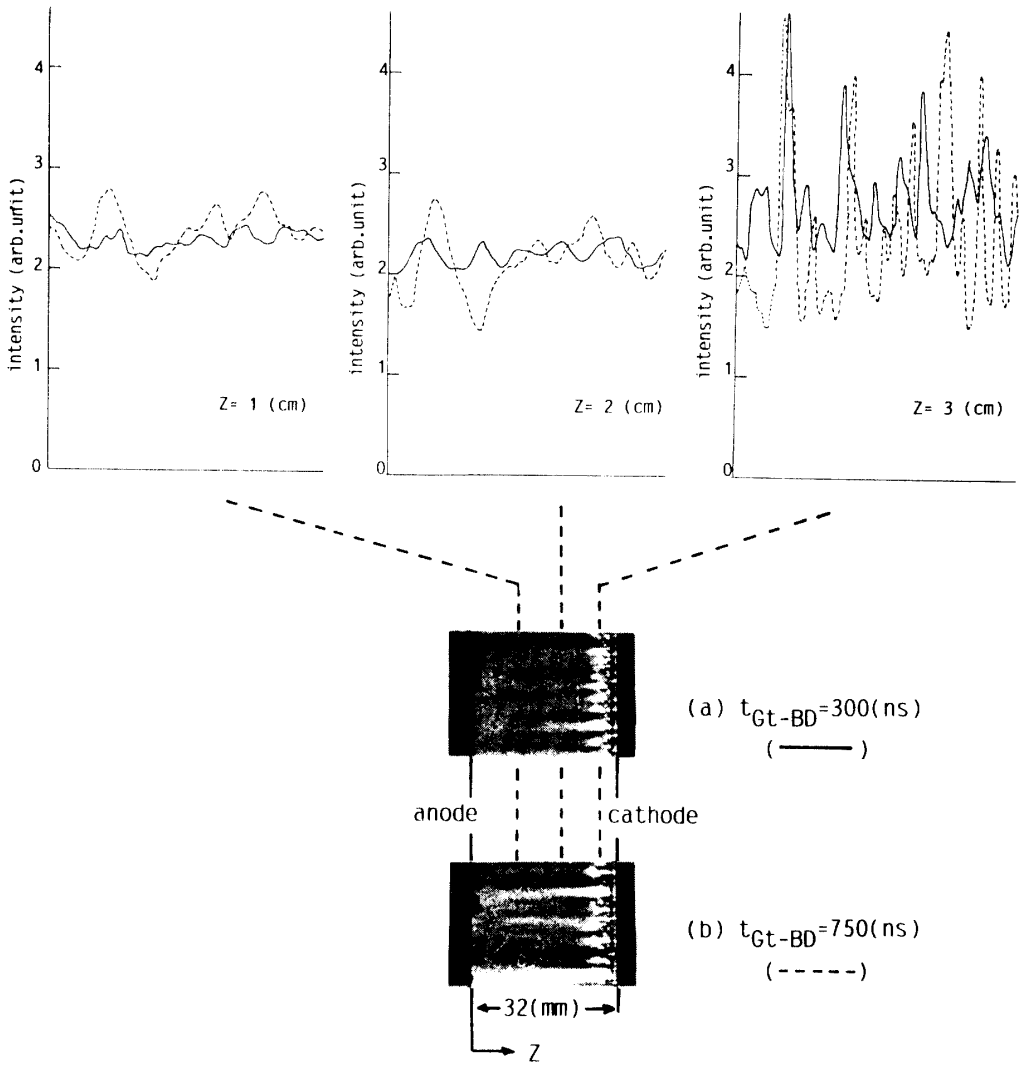

Fig. 6. Spatial distribution and time-integrated photographs of radiation intensity along the glass tube at (a) $t_{Gt\text{-}BD}$ = 300 ns and (b) $t_{Gt\text{-}BD}$ = 750 ns.

electrons diffuse and disappear before the main discharge. On the other hand, if the delay time $t_{Gt\text{-}BD}$ is too short, primary electrons are not homogeneously scattered on the cathode and the electrical field on the cathode isn't reduced enough to suppress the glow-to-arc transition.

Fig. 8(a) and (b) show the contour lines of both glow-to-arc transition rate and laser output as functions of the electrical charge Q_h and Q_e. The experimental values underlined in the figures are obtained with the normal operation. Similar to the result of Fig. 7, it is seen from Figs. 8(a) and (b) that the suppression of the glow-to-arc transition leads to the increase of the laser output. In Fig. 8(a), it is found obviously that there is the minimum of Q_h to suppress the glow-to-arc transition at less than a certain rate. For example, it requires 6.6 (μC) as the minimum of the electrical charge Q_h (i.e. Q_{hmin}) to suppress the transition at less than a rate of 15(%). The appearance of the minimum of Q_h, Q_{hmin}, is considered as follows. In the case that Q_h is smaller

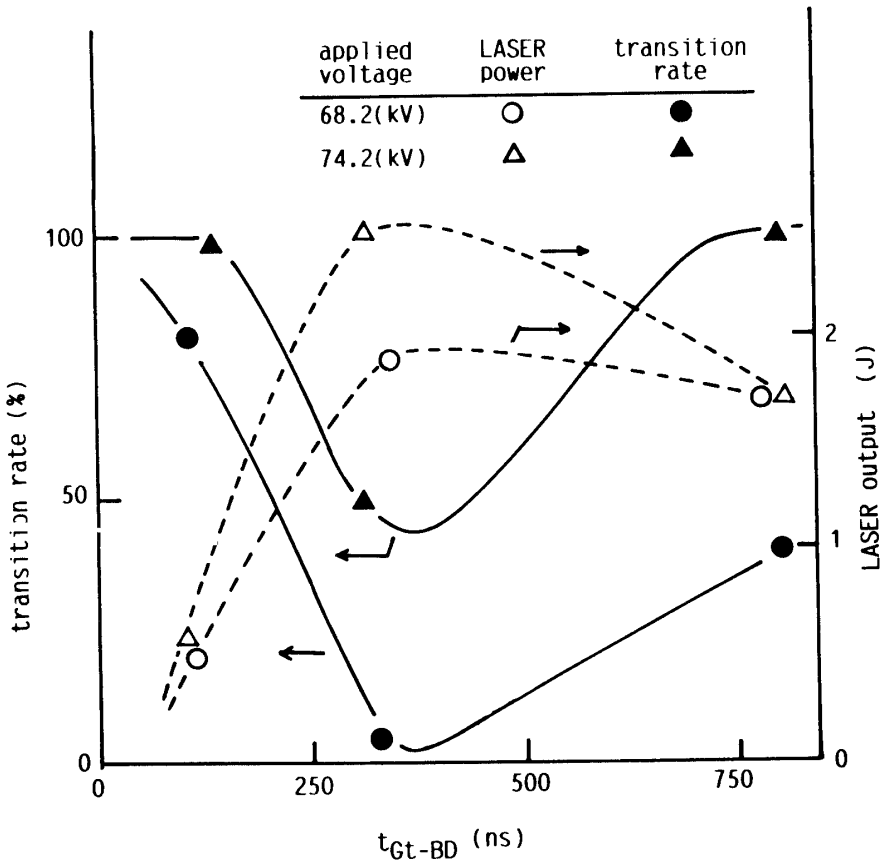

Fig. 7. Transition rate and laser output versus delay time $t_{Gt\text{-}BD}$ for various applied voltage.

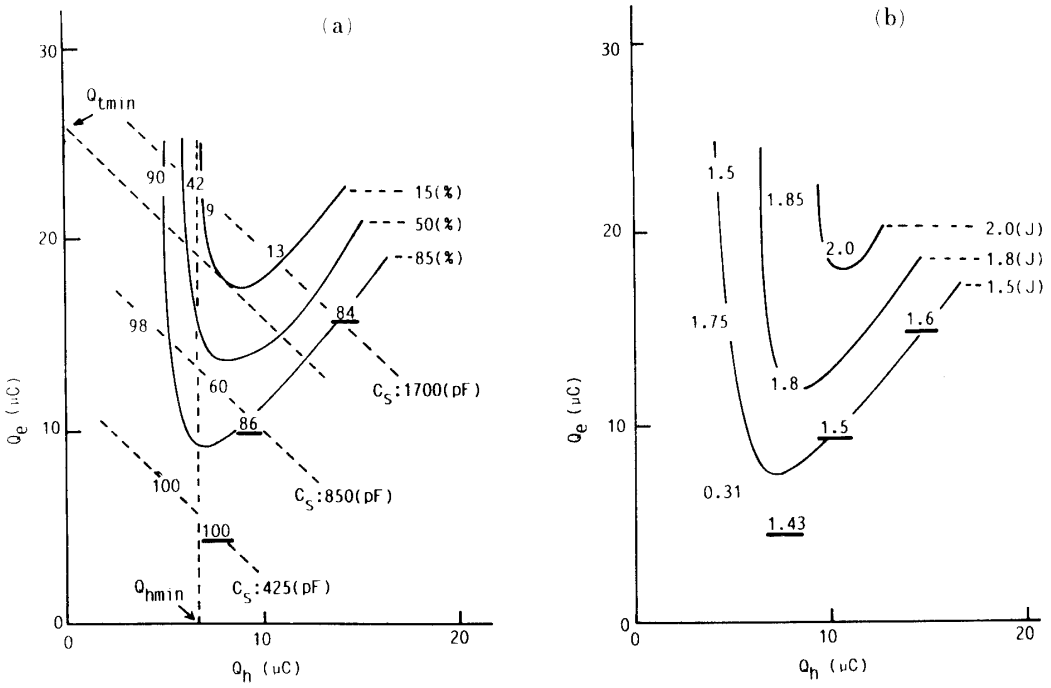

Fig. 8. Contour lines of (a) glow-to-arc transition rate and (b) laser output as functions of electrical charge Q_h and Q_e.

than Q_{hmin}, because the reduction of the electrical field by the preionization before the closure of the gap G_t is insufficient, the streamer from the cathode developes and it is impossible to suppress the transition at less than a certain rate even though Q_e infinitely enlarges.

Next, we study on the way to minimize the whole electrical charge, Q_t, for the preionization. As shown in Fig. 8(a), because the slope of each broken straight line fitting the experimental values at the same capacitance C_s is about minus one, the relation between Q_h and Q_e is expressed by the following equation.

$$Q_h + Q_e = C(C_s) \tag{2}$$

$C(C_s)$: a constant C which depends on the capacitance C_s

So the constant C equals to Q_t, and is represented as the interception on the vertical axis in Fig. 8(a). The minimum of Q_t to suppress the glow-to-arc transition at less than a certain rate is obtained by the value of the interception when the broken straight line expressed by equation (2) is in contact with the area at less than the rate in Fig. 8(a), and then Q_h and Q_e are obtained by the co-ordinates of the point of the contact. For example, the minimum of Q_t (i.e. Q_{tmin}) to suppress the transition at the rate of less than 15(%) is about 25.7 (μC), and Q_h and Q_e are about 7.7 (μC) and 18.0 (μC), respectively.

In this way, it is possible to design the TCC circuit so as to minimize the amount of the electrical charge for preionization. In the normal operation, it is difficult to obtain the values of Q_h and Q_e required for more stable discharge as shown in Fig. 8(a). So the gap G_t in the TCC circuit is effective for the suppression of the glow-to-arc transition.

3.4 Conclusions

The homogenous glow discharge is obtained by scattering the primary electrons on the surface of the cathode. But the glow-to-arc transition is apt to occur as the input energy density; i.e. input energy per unit volume to active region increases. We examined the new method using "TCC circuit" for the control of the preionization and it was confirmed that the glow-to-arc transition can be suppressed by this method.

There is the optimum delay time between the initiation of fire of the gap G_t and the initiation of the main discharge. It is considered that it is attributable to the distribution of the primary electrons in the space of the main electrodes.

The transition can be suppressed by the control of the Q_h and Q_e which are amount of the electrical charge injected into the TCC circuit before and after the fire of the gap G_t, and further it is showed how to minimize the charge Q_t which is the total electrical charge into TCC circuit for preionization.

In this experiment, the air gap is used as the gap G_t, and the triggering time can be controlled to vary the gap spacing by the micrometer-head, but it is more suitable for the practical application to use a thyristor as the gap G_t from the point of view

of controllability and reliability. In future, the discharge operation with high repetition rate to produce the plasma is required for this study.

4. Direct Energy Conversion from Laser Energy to Electricity with Laser-Produced Plasma

4.1 Principle of direct energy conversion with laser-produced plasma

The principle of energy conversion from laser to electricity is shown in Fig. 9. At first, the laser beam is irradiated on a solid target in a vacuum chamber to produce the plasma, and the laser energy is converted to the kinetic energy of the produced plasma. The produced plasma expands and enters into a PDC (Plasma Direct Converter). Both ions and electrons are included in the plasma but the mass of an ion is very large compared with that of an electron. Therefore, the ion kinetic energy is very large compared with the electron's kinetic energy. Since the ions carry most of the kinetic energy of the plasma, it is attracted the attention for the PDC to convert only the ion's kinetic energy to electricity. The electrons in the plasma which enter into the PDC are repelled by the suppressor grid which has an applied negative voltage to separate ions and electrons electrostatically. The ions are decelerated by the field between the suppressor grid and the ion collector to which is applied a positive voltage, and some of the ions reach the ion collector. The induced current flows between the suppressor grid and the ion collector until the ions reach the collector and electrical energy is taken out by the external load. In this experiment the positive bias potential V_C is connected to the external circuit as an imaginary load and it is satisfied to be $V_C I_C \gg I_C R^2$. Here I_C is the collector current which passes through the imaginary load. In this experiment, the PDC which has two collectors as shown in Fig. 10, is used [*16*]. The first collector is applied low positive voltage V_V and the second one is applied higher voltage V_C so that slow ions are caught by the first collector and fast ions which have high energy are caught by the second one. The ions which aren't decelerated enough collide with the ion collectors and the kinetic energy of ions is lost on the collector surface as the thermal energy. If there are many collectors, each ion can be caught by each collector applied desirable voltage which fits each ion's kinetic energy. So the kinetic energy of the ions is converted effectively to the electric energy because the loss of the thermal energy on the collectors decreases.

4.2 Experiments of direct energy conversion from laser energy to electricity

4.2.1 Dependence of energy conversion efficiency on laser energy

In this section, the dependence of the efficiency of η_1, η_3 and $\eta_1\eta_3$ on the laser energy is described. Where η_1 and η_3 are the conversion efficiency from the laser energy to the kinetic energy of ions and from it to the electric energy respectively. The experimental apparatus is shown in Fig. 11. Both carbon and cross-linked polyethylene (XLPE) are used as targets. The laser output is about 8J/pulse at maximum

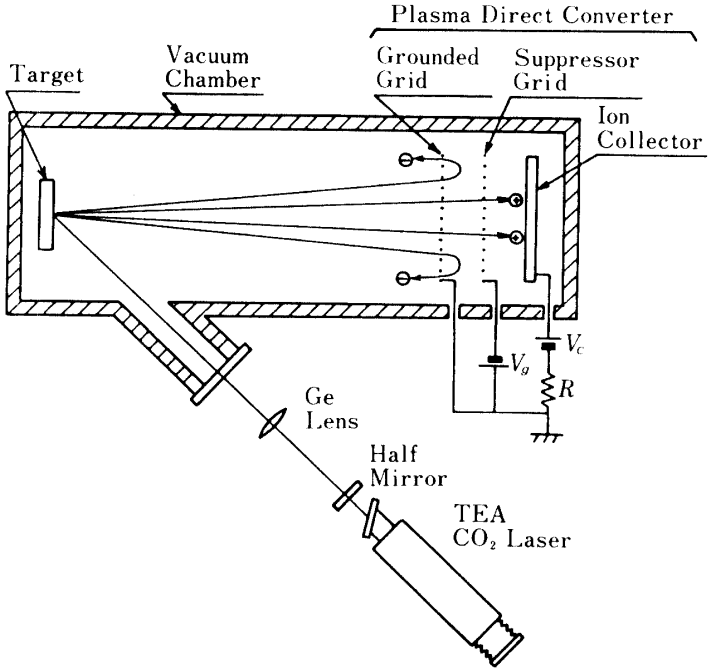

Fig. 9. Principle of energy conversion from laser energy to electricity.

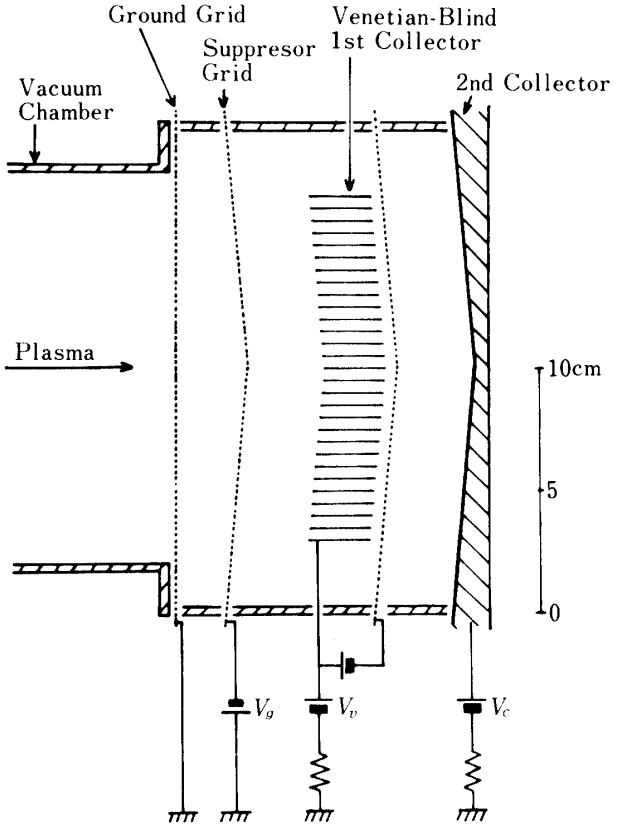

Fig. 10. The PDC with two collectors.

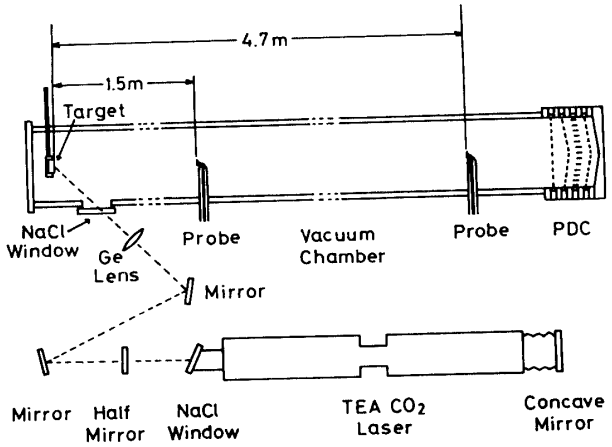

Fig. 11. Experimental apparatus.

and the fullwidth at half maximum of the laser pulse is about 150 ns.

At first, the method of measuring η_1 is explained. The laser energy is measured by a calorimeter. The ions' kinetic energy is measured by the Langmuir probe set at 1.5 m from the target surface. Firstly the voltage V_p is applied on the probe and the time variation of the probe current is measured. These waveforms of measured probe current for different applied voltage V_p are read and V_p-I_p characteristics at each time are obtained as shown in Fig. 12. The ion saturation current I_{si} at each time is obtained from the V_p-I_p curve and the ion density n is calculated by the following equation

$$n = I_{si} / Sev \tag{3}$$

where S is the area of the probe, e is the electric charge of an electron and v is the expansion velocity of ions, but the number of electric charge of an ion Z is assumed to be 1. The ion density changes with time, so the ion density calculated from equation (3) is integrated temporally and spatially to obtain the number of ions by the next equation.

$$N_p = \sum_{i=1}^{n} \int_0^{\pi/2} \int_0^{2\pi} \int_L^{L+v_i \Delta t} n_i K(\theta) r^2 \sin\theta \, dr d\varphi \, d\theta \tag{4}$$

Here the polar coordinates is set at the center of the target as shown in Fig. 13 and the ion density at r=L, $\theta = 0^\circ$ is a standard value. In equation (4) the sampling is done at constant intervals Δt ($\simeq 1\ \mu s$) and the integration with time is done by the summation each value. The values of n_i and v_i are the ion density and the expansion velocity of the ith group of ions. The $K(\theta)$ is the coefficient of the angle dependence of the expansion plasma. Experimental results show that

$$K(\theta) \simeq \cos\theta \tag{5}$$

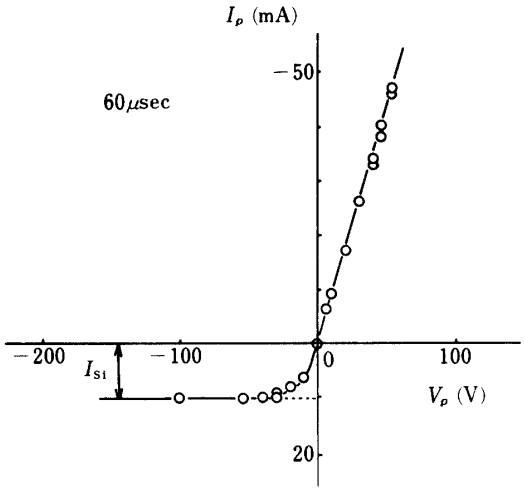

Fig. 12. A typical $V_p - I_p$ characteristics.

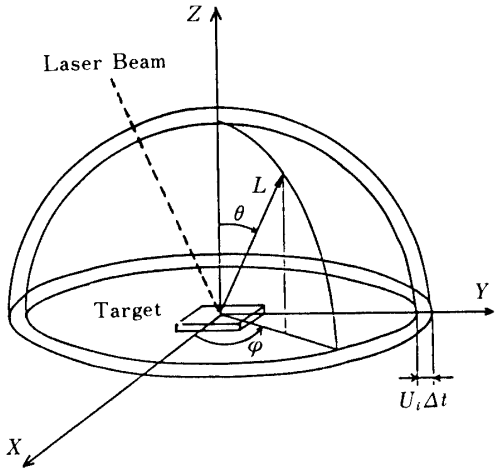

Fig. 13. Polar coordinates used for the calculation.

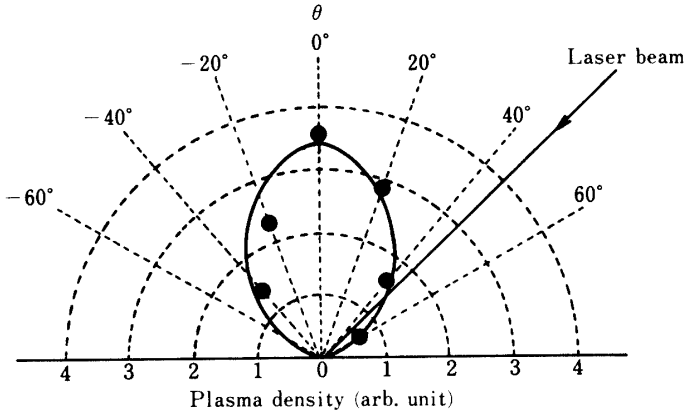

Fig. 14. Angle dependence of the expansion plasma.

as shown in Fig. 14. The kinetic energy of each ions group is given by $mv_i^2 n_i/2$ (m is the mass of an ion), therefore the kinetic energy of the expansion ions E_p is obtained from the next equation.

$$E_p = \sum_{i=1}^{n} \int_0^{\pi/2} \int_0^{2\pi} \int_L^{L+v_i\Delta t} \frac{1}{2} m v_i^2 n_i K(\theta) r^2 \sin\theta \, dr \, d\varphi \, d\theta \tag{6}$$

In this way, the conversion efficiency η_1 is calculated by the ratio of the kinetic energy E_p given by equation (6) to the laser energy. Next, the method of measuring η_3 which is the conversion efficiency in the PDC from the incident ions' kinetic energy to the electric energy is explained. The kinetic energy of the incident ions on the PDC is measured by the Langmuir probe set at 4.7 m from the target surface. The electric energy converted by the PDC is calculated by the following equation.

$$E = V_c I_{cmean} t_c + V_v I_{vmean} t_v \tag{7}$$

Where V_C and V_V are the applied voltage of each collector, I_{cmean} and I_{vmean} are the mean value of the current of each collector and t_C and t_V are the duration of each collector current. The conversion efficiency η_3 in the PDC is calculated by the ratio of the electric energy given by equation (7) to the energy given by equation (6) at 4.7 m from the target.

4.2.2 Experimental results and discussion

The dependence of $\eta_1\eta_{3max}$ on the laser energy using the PDC with two collectors is shown in Fig. 15. The η_3 varies with the collector voltage and is maximum at the proper voltage. The total conversion efficiency from the laser energy to the electric energy is described by

$$\eta_{total} = \eta_1 \eta_2 \eta_3 \tag{8}$$

Where η_2 is the ratio of the incident ions on the PDC to the expansion ions from the target and it is very small $\eta_2 = 2.69 \times 10^{-4}$ in this apparatus. If the PDC is distributed around the target hemispherically as shown in Fig. 16, it is satisfied to be $\eta_2 \simeq 1$ and η_{total} is given by

$$\eta_{total} \simeq \eta_1 \eta_3 \tag{9}$$

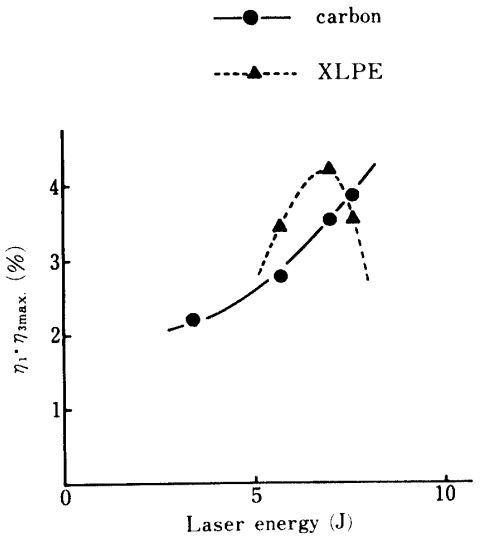

Fig. 15. Dependence of $\eta_1 \eta_{3\max}$ on laser energy.

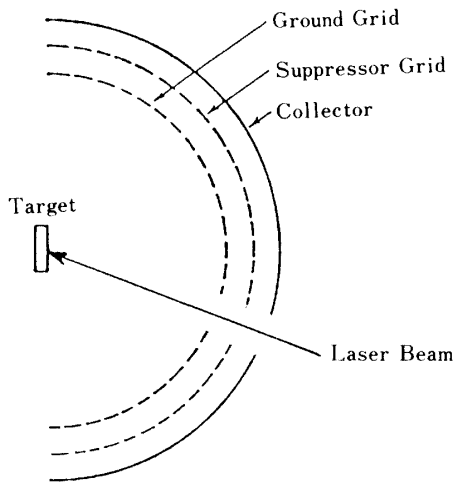

Fig. 16. The PDC distributed around the target hemispherically.

Therefore $\eta_1 \eta_{3\max}$ is shown as the total conversion efficiency for the PDC in the future. The $\eta_1 \eta_{3\max}$ increases with the laser energy using the carbon target as shown in Fig. 15. But when the XLPE target is used, $\eta_1 \eta_{3\max}$ increases with the laser energy at first and reaches maximum and secondly it decreases with the laser energy. The laser energy is expected to be larger for the practical use in the future, so the properties of the carbon target used are desirable because $\eta_1 \eta_{3\max}$ increases with the laser energy. Next the properties of the XLPE target which has the maximum value for $\eta_1 \eta_{3\max}$ are discussed. The Fig. 17 shows the dependence of η_1 on the laser energy. The η_1 of the XLPE is smaller than that of the carbon and each of the two increases with the laser energy. Therefore it is considered that the properties of $\eta_1 \eta_{3\max}$ using the XLPE which has the maximum is due to the properties of η_3. So the conversion efficiency η_3 is considered. In the PDC, the suppressor grid separates the incident ions and electrons electrostatically and only the kinetic energy of the ions is converted to electricity. The interval of the mesh of the suppressor grid should be very much smaller than the Debye length of the plasma to separate the ions and electrons electrostatically. Therefore the interval of the mesh 1 and the Debye length λ_D are compared. The interval of the mesh is l = 0.77 mm and the Debye length λ_D is calculated by

$$\lambda_D = 7400\sqrt{T_e(eV)/n_e(\mathrm{cm}^{-3})} \qquad (\mathrm{mm}) \qquad (10)$$

Where T_e is the electron temperature and n_e is the electron density. If the plasma's neutralization condition is satisfied, $n_e = \Sigma\, n_i Z$ where n_i is the ion density, so $\Sigma\, n_i Z$ (= n_i, if Z=1 is assumed) is used instead of n_e to calculate λ_D. The electron temperature T_e is about 10 eV for both XLPE and carbon targets. The dependence of the ion density on the laser energy is shown in Fig. 18. The XLPE plasma isn't easily

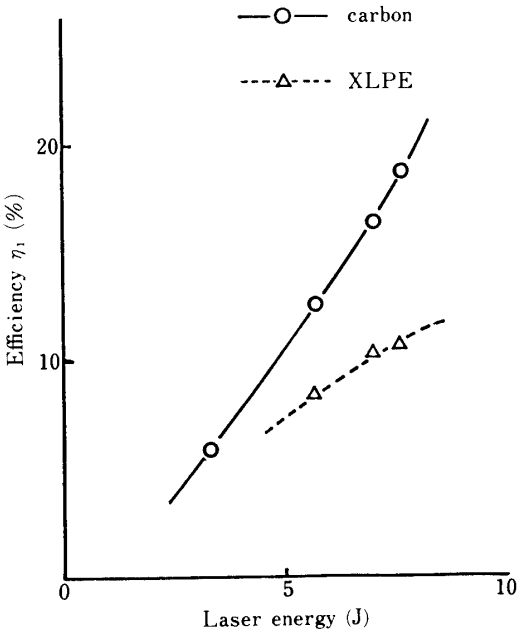

Fig. 17. Dependence of η_1 on laser energy.

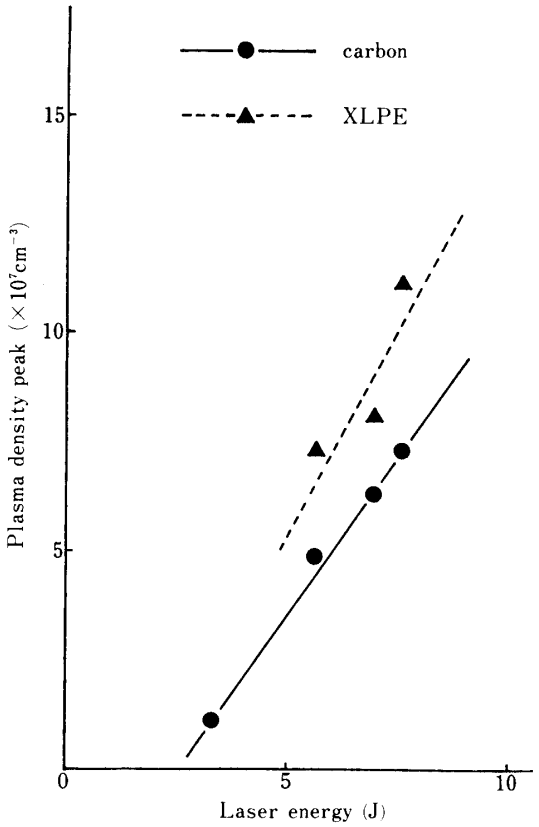

Fig. 18. Dependence of ion density on laser energy.

separated electrostatically because the ion density for the XLPE target is larger than that of the carbon as shown in Fig. 18 and the Debye length for the XLPE target is smaller than that of the carbon target. The relation between the conversion efficiency η_3 and the Debye length λ_D is shown in Table 3. The $\eta_{3\max}$ is 40% ($\lambda_D/l = 3.55$) and 41% ($\lambda_D/l = 3.38$) at the laser energy 5.7 J and 7.0 J respectively. The $\eta_{3\max}$ varies little because λ_D/l is almost same. But $\eta_{3\max}$ decreases when the laser energy is increased more because the ion density becomes larger and electrostatic separation isn't as effective. So, the maximum efficiency of $\eta_{3\max}$ = 33.3% is obtained for $\lambda_D/l = 2.86$ at the laser energy of 7.6 J. The properties of $\eta_1\eta_{3\max}$ mentioned above are obtained because $\eta_{3\max}$ decreases in this manner.

Table 3. Relation between the conversion efficiency η_3 and the Debye length.

Laser energy (J)	Ion density (peak) ni ($\times 10^7 cm^{-3}$)	Debye length (min.) λ_D (mm)	Rate of λ_D to 1 λ_D/l	Conversion efficiency of PDC η_3 (%)
5.7	7.33	2.73	3.55	40.8
7.0	8.10	2.60	3.38	41.0
7.6	11.3	2.20	2.86	33.3

4.2.3 Measurements of the ionization rate of laser-produced plasma

The conversion efficiency of each part of the energy conversion from laser beam to electricity is discussed above. The ionization rate of the laser-produced plasma is measured in this chapter to understand the state of the plasma. The experimental apparatus is shown in Fig. 11. Carbon and the XLPE are used as targets. The ionization rate x is defined by

$$x = N_p / N_v \tag{11}$$

Where N_p is the number of ions and N_V is the number of vaporized particles from the target (N_V = the number of ions + the number of neutral particles). The number of ions is measured by the Langmuir probe set at 1.5 m from the target surface using equation (4). The number of vaprozied particles is measured as follows. About 200 – 1000 shots of the laser beam are irradiated on the target to measure the vaporized mass, and the number of vaporized particles is calculated by

$$N_v = N_A M / m \tag{12}$$

Where N_A is the Avogadro number, M is the mean vaporized mass of the target at one shot and m is the atomic weight of the target (in case of the XLPE, the ratio of the carbon to the hydrogen is assumed to be 1 to 2, therefore the mean value m = (12 + 1 + 1)/3 = 4.67 is used.). The Fig. 19 shows the dependence of the ionization rate on the laser energy. The ionization rate increases with the laser energy using each target. The ionization rate of the XLPE target is about 10 times smaller than that of the carbon. It is supposed that this is due to the difference of the melting point of each

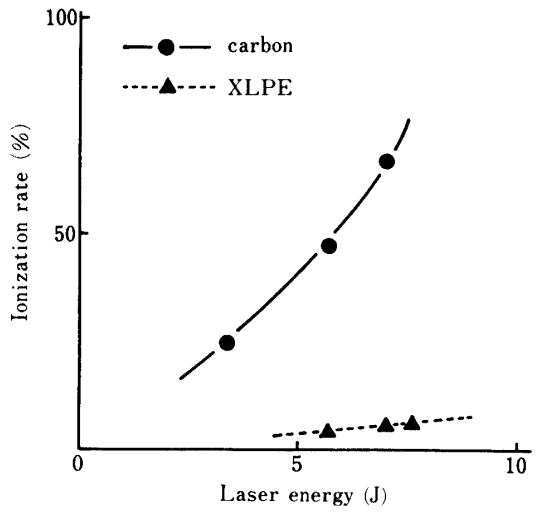

Fig. 19. Dependence of ionization rate on laser energy.

target. The melting point of the XLPE is about 100°C and that of carbon (graphite) is about 3500°C. So the ionization rate of the XLPE is small because many neutral particles are vaporized by the laser beam before the ionized plasma is produced. The ionization rate of plasma is needed to be large because the PDC doesn't convert the kinetic energy of neutral particles.

4.2.4 Considerations of targets and laser-produced plasma

Carbon and XLPE are used as targets in this experiment. We now considered, from the experimental results, what is the best target for this energy conversion from laser energy to electricity.

As is described in 4.2.1, it is better that the ion density is small because the Debye length λ_D should be large to separate the ions and electrons electrostatically in the PDC. In other words, if there are two kinds of plasma and each plasma has the same ion kinetic energy, it is better that the ion density is small for the electrostatic separation. Therefore a desirable plasma is considered to satisfy the following conditions.

(1) ion density is small
(2) mass of an ion is large
(3) velocity of ions is large

(2) and (3) are given because such plasma has the same kinetic energy with smaller ion density. The ions of the plasma produced with carbon target are only carbon ions, and it is supposed that in the plasma produced with the XLPE there are carbon ions and hydrogen ions in the ratio of 1 to 2. A hydrogen ion is almost 10 times lighter than that of a carbon ion. So it is supposed enough that there are a lot of light hydrogen ions in the plasma produced with the XLPE. The Fig. 20 shows the dependence of the ion (plasma) density on velocity. The ion density with the XLPE is larger than that

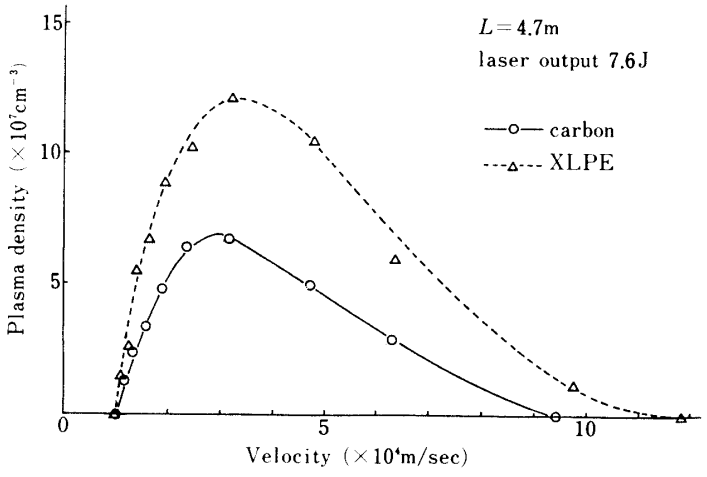

Fig. 20. Dependence of ion density on velocity.

with carbon but the ion (plasma) velocity with the XLPE isn't much larger than that with carbon. In other words, light hydrogen ions are expected to accelerated by laser energy but they aren't accelerated too much. Therefore heavy materials are expected to be good targets for the PDC. Next, the following plasma is good according to the results shown in the session of 4.2.2.

(4) ionization rate is large

The ionization rate with carbon target is 10 times larger than that with the XLPE, so the ionization rate seems to vary so much with target materials. It is important to select the target materials in point of view the ionization rate. As mentioned above, it is one of the problems to select a target which satisfies the conditions (1)–(4).

4.3 Conclusions

The results obtained in this experiment are as follows.

(1) When the XLPE is used as a target, the ion density increases with laser energy and the electrostatic separation isn't achieved completely and the conversion efficiency in the PDC $\eta_{3\max}$ has a maximum value at some laser energy.
(2) The ionization rate of the plasma increases with laser energy. The ionization rate of the plasma at the laser energy of 7.0 J is 67.1% using carbon target and 5.9% using the XLPE target.
(3) Heavy materials are expected to be good targets.
(4) The $\eta_1\eta_{3\max}$ increases with laser energy using carbon target.

5. Energy Conversion with Surface Magnetic Field with Geometric Mirrors

5.1 Introduction

Fundamental experiments for the confinement of laser-produced plasma by the magnetic field with geometric mirrors have been done. Only the kinetic energy of ion particles in the plasma was used for the direct energy conversion. This plasma confinement by surface magnetic field was proposed by Wong et al. [*17*]. In this method, as plasma is confined in the field-free region surrounded by the magnetic wall, the energy loss due to a synchrotron radiation is expected to be very small and the required energy for the confinement is also very small. So far the experiments on linear surmac and troidal surmac have been reported [*18*] [*19*]. Theory on plasma confinement by surmac with geometric mirrors which have smaller diameters at both ends compared with that at the center has been discussed, and the experimental results on the confinement of the direct current discharge plasma by surmac of which diameter decreases sharply with distance from the center of surmace have been reported [*20*] in detail. On the other hand, recently big tandem-mirror devices have been constructed to confine the plasma. In these devices, it has been reported that plasma is confined by ambipolar potential [*21*] [*22*] which is made by two mirrors field at both ends. Therefore, the

research of ambipolar potential generated in plasma by these devices has become important to investigate the process of potential generation.

We have produced plasma by focusing the output beam of a TEA CO_2 laser on the XLPE plane target which is set in the surmac. We have measured the confinement of produce plasma and the plasma potential of it. Particularly we are interested in the production process of plasma potential with time and whether the potential is the same kind of one measured by the conventional mirror experiments.

5.2 Experimental apparatus and procedure

The experimental setup is shown in Fig. 21. A TEA CO_2 laser beam with output energy of 1 J and pulse duration of 40 ns (full-width at half maximum) is focused on the XLPE plane target. The coil current for the generation of magnetic field reaches maximum value at 0.3 ms after it is triggered and decreases slowly with an e-folding time of 1.2 ms. The coil current is synchronized to be maximum with the pulse of the TEA CO_2 laser by a pulse generator and delay pulser. The pressure of vacuum chamber in which the coil for the surmac and the plane target are installed is about 7×10^{-6} Torr.

The generation process of laser plasma is observed by the time integrated photograph and the image converter camera (Hadland IMACON 790). Ion saturation current, plasma potential and so on are measured by a Langmuir probe located in the surmac coil. The spatial distribution of ion saturation current is measured, moving the prove along the axis of the vacuum chamber. We call hereafter Z and R directions for the axial and the radial direction respectively as shown in Fig. 21. The probe signals triggered by the applied voltage of the TEA CO_2 laser have been measured and the pre-trigger of 5 μs has been set for the measurements. The time of pre-triggered point is t = 0.

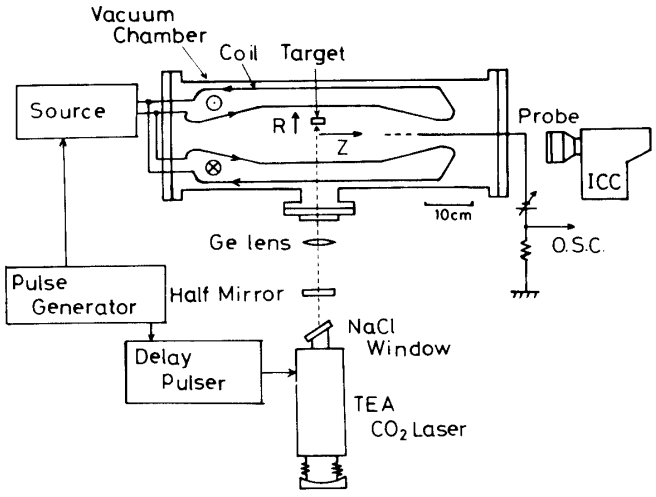

Fig. 21. Experimental set up for the surface magnetic confinement.

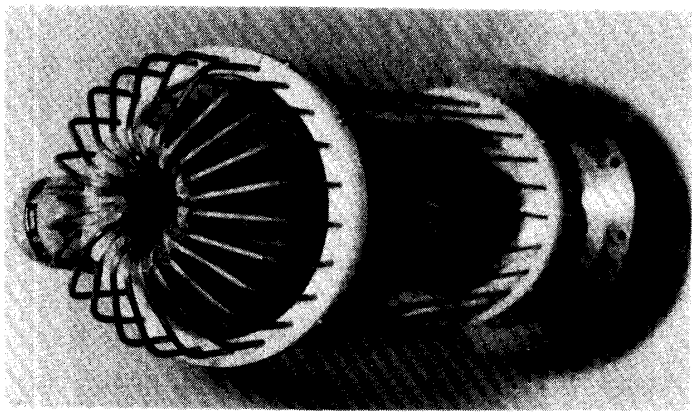

Fig. 22. Photograph of the magnetic coil.

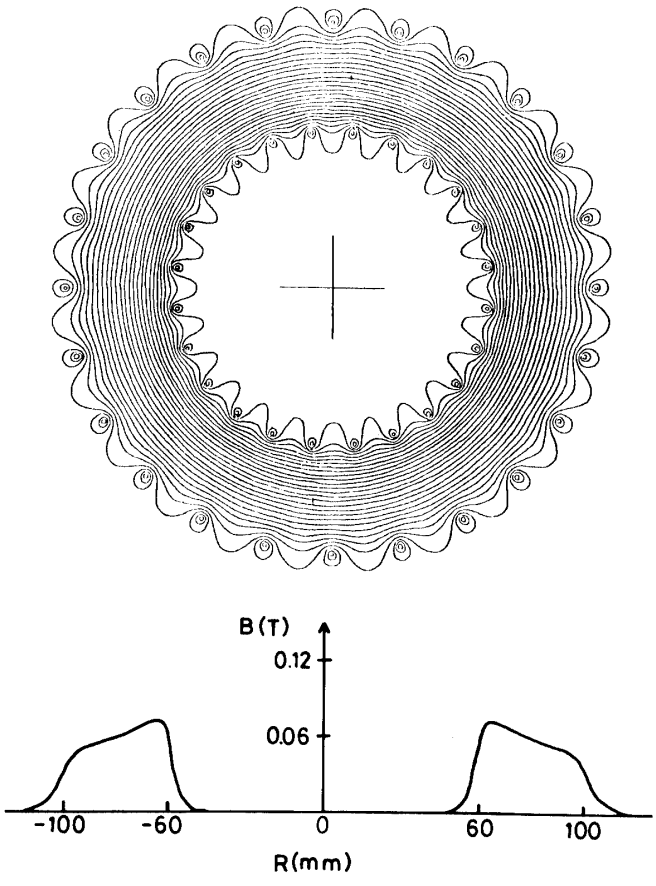

Fig. 23. Calculated distribution of the magnetic line of force at the central cross section of the surmao coil (a) and the calculated magnetic flux density at the coil current I_b = 1000 A (b).

The 48-poles surface magnetic field is produced by 24 sets of current rods which are set with two layers along the wall of the vacuum chamber. The inner and outer diameters of the coil are 12 cm and 20 cm at the central region respectively and the intensity of the magnetic wall is about 600 gauss at the coil current of 1000 A. The photograph of the coil for the surface magnetic field is shown in Fig. 22. The inner diameter of the coil decreases with distance Z from the axial center with the gradient of $dR/dZ = 0.25$ in order to reduce the end loss and becomes 6 cm at the ends of $Z = 28$ cm. The Fig. 23(a) shows the calculated distribution of the magnetic line of force at the central cross section of the surmac coil. The Fig. 23(b) shows the calculated magnetic flux density at the coil current of $I_b = 1000$ A. There are a large free field region inside of the coil and a magnetic wall at the circumference.

5.3 Experimental results

5.3.1 Observation of generation process of laser-produced plasma by image converter camera

The framing-mode pictures of the generation process of laser-produced plasma (bottom), laser output waveform (top) and typical waveform of the saturation current (middle) measured at the same time are shown in Fig. 24(a). The laser output waveform is measured by monitoring the reflected beam of the TEA CO_2 laser from a NaCl brewster window with a Au-Ge semiconductive detector cooled at 77 K. The value of laser output shown is arbitrary unit and the time scale of laser output waveform and ion saturation current is same. The ion saturation current I_{si} is measured by Langmuir probe applied -90 V at the distance of about 3 cm from the target. Two groups in laser-produced plasma which form the first and the second peaks on the saturation current waveform respectively are observed. This indicates that the laser-produced plasma expands forward forming two groups. The pictures shown in Fig. 24(a) are taken at framing rate of 1×10^6 frames per second. In each frame, a white circular luminous part shows the laser-produced plasma and a white rectangular part at the right side is the target. The first peak of the ion saturation current, and the laser-produced plasma in the third frame is smaller compared with the plasma in both the second and the forth frames. The plasma in the third frame corresponds to a part between the first and the second peaks of the ion saturation current. After the forth frame, the second peak of the ion saturation current appears. The photograph of the streak mode taken at 3 cm from the target by the image converter camera is shown in Fig. 24(b). In the photograph, two luminous parts are observed. These results indicate that the laser-produced plasma forming two groups are generated.

5.3.2 Effect of magnetic wall on plasma confinement

The axial distribution of ion saturation current I_{si} measured by Langmuir probe is shown in Fig. 25. The applied voltage on the probe is -90 V. The Fig. 25(a) and (b) are measured at the coil current of $I_b = 0$ and 1150 A (this corresponds to $B \simeq 0.08$ T) respectively. The symbols of x10, x5, x2, and x1 which are written at the right

side in each waveform represent the factor of times of the vertical values compared with the reference value written with x1. It is found from Fig. 25(a) that the first peak propagates instantly and the second one propagates gradually compared with the first one along the axial direction. The peak values and duration of the second peak of ion saturation current with magnetic field (Fig. 25(b)) become larger compared with the values without magnetic field (Fig. 25(a)). It seems due to the reflection of plasma at the magnetic wall. The arrival time of the first and the second peaks at each point

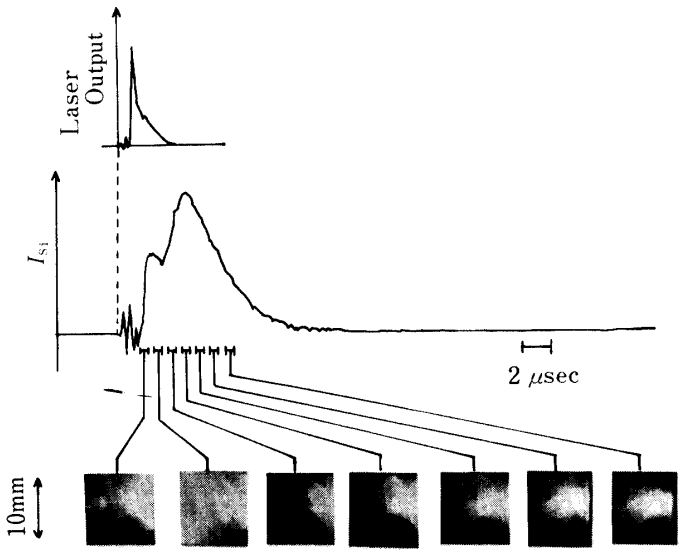

(a)

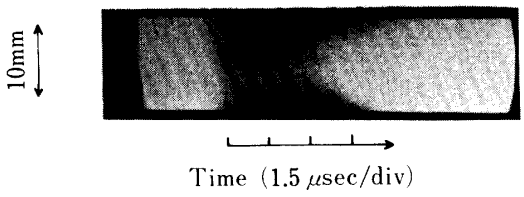

(b)

Fig. 24. Laser output (top), typical waveform of the saturation current (middle) and framing-mode pictures taken at intervals of 1 μs and framing rate of 1×10^6 frames per second for the generation process of laser-produced plasma (bottom) (a) and the photograph of the streak mode taken at 3 cm from the target (b).

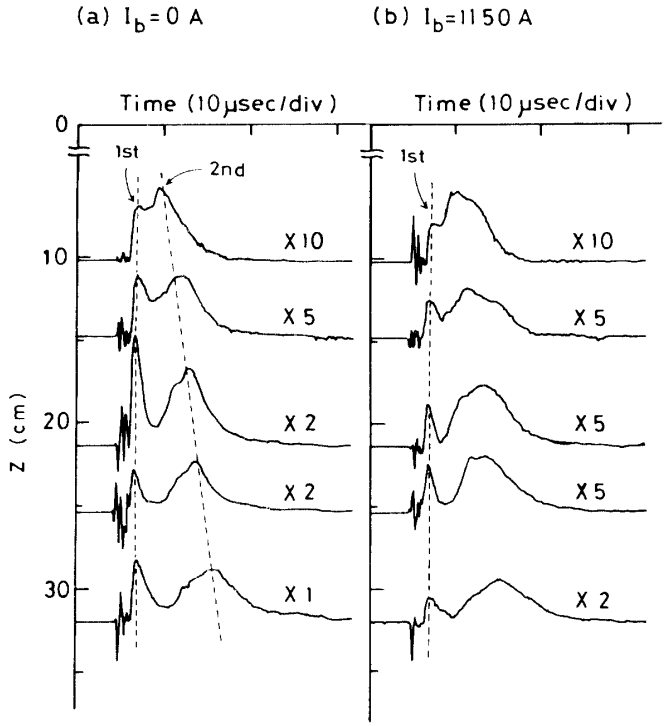

Fig. 25. Axial distribution of ion saturation current I_{si} as a function of time with (a) and without (a) magnetic field.

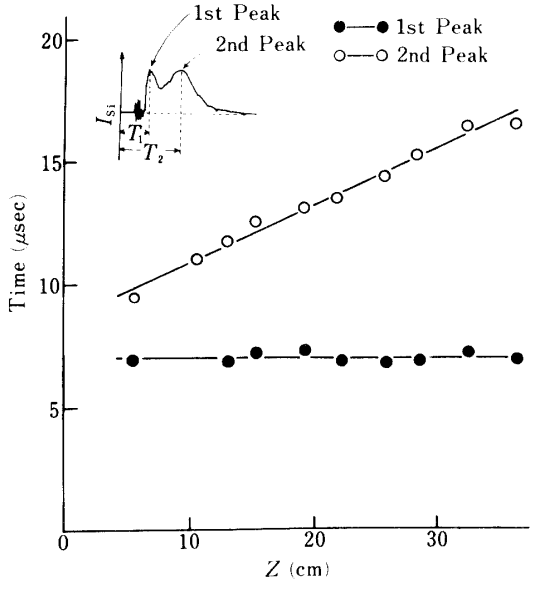

Fig. 26(a) Arrival time of the first and the second peaks of ion saturation current with position along the Z-direction.

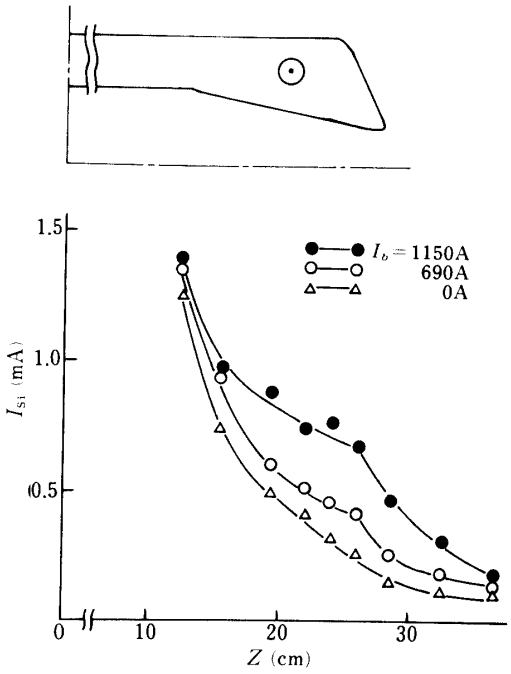

Fig. 26(b) Configuration of surmac coil (upper) and the axial distribution of the second peak (lower).

along the Z-direction is shown in Fig. 26(a). Here, the pre-trigger pulse is used as the origin of time. Almost the same time of 6.9 μs at each point is observed for the first peak and the time for the second peak is longer compared with that of the first peak and varies linearly with the distance. This indicates that the first peak has much higher energy than that for the second peak. Because of this higher energy, we need much stronger magnetic field to confine the plasma of the first peak. Therefore, we cannot observe the confinement of it in this experiment. The axial distribution of the second peak (lower) and the configuration of the surmac coil (upper) are shown in Fig. 26(b). The peak values with magnetic field (I_b = 1150 A and 690 A) are larger than that without magnetic field. This increasing with magnetic field is due to the reflection of the plasma at the magnetic wall and the increasing of ion saturation current with magnetic field near the end of the magnetic coil (Z=20–25 cm) is larger compared with at the central part of the coil ($Z \leqq 15$ cm). In case of no magnetic field the peak value decreases gradually with distance Z, but, in case with magnetic field the value decreases gradually to the point of $Z \simeq 26$ cm and decreases rapidly from that point forward outside because of no existance of magnetic field.

5.3.3 Potential formation of plasma in the surmac

The Langmuir probe is used to measure the plasma potential Φ_s, electron temperature T_e and plasma density n. The laser plasma is produced many times and the applied voltage V_p on the probe is changed and the probe current for each plasma is measured. The signal from the probe which is set at the fixed position is used for the reference to reduce the uncertainty due to the lack of complete reproducibility of plasma production by successive laser firing. The characteristics of laser-produced plasma at some fixed time are measured and the plasma potential Φ_s, electron temperature T_e and plasma density n are obtained from these results. The probe current measured at the point of R = 0 and Z = 22.7 cm by varying the probe voltage V_p is shown in Fig. 27. The figures of (a) and (b) are without and with magnetic field respectively. In Fig. 27(a) the polarity of probe current changes completely from positive to negative as the bias voltage V_p is varied from –6.5 V to +6.5 V. This indicates that the maximum value of plasma potential is positive a little. On the other hand, in Fig. 27(b) as the voltage V_p is varied from –6.5 V to +6.5 V, the polarity of probe current at about 18 μs is positive. This indicates that the plasma of large positive potential is generated at around this time. The time evolution of T_e, n and Φ_s at both points Z = 22.7 cm and 35.9 cm without magnetic field is shown in Fig. 28(a). The plasma density reaches maximum value at about 14 μs (Z = 22.7 cm) and 18 μs (Z = 35.9 cm) respectively. Each maximum plasma density corresponds to the second peak described in section 5.3.2. The obtained maximum plasma density is the order of 10^{10} cm^{-3} and the plasma potential at Z = 22.7 cm reaches maximum value of about 10 V at about 15 μs and decreases afterward. The maximum value of plasma potential at Z = 35.9 cm is about 6 V. The time evolution of T_e, n, and Φ_s at Z = 22.7 cm and 35.9 cm with magnetic field is also shown in Fig. 28(b). The positions Z = 22.7 cm and 35.9 cm are inside and outside of the magnetic coil respectively.

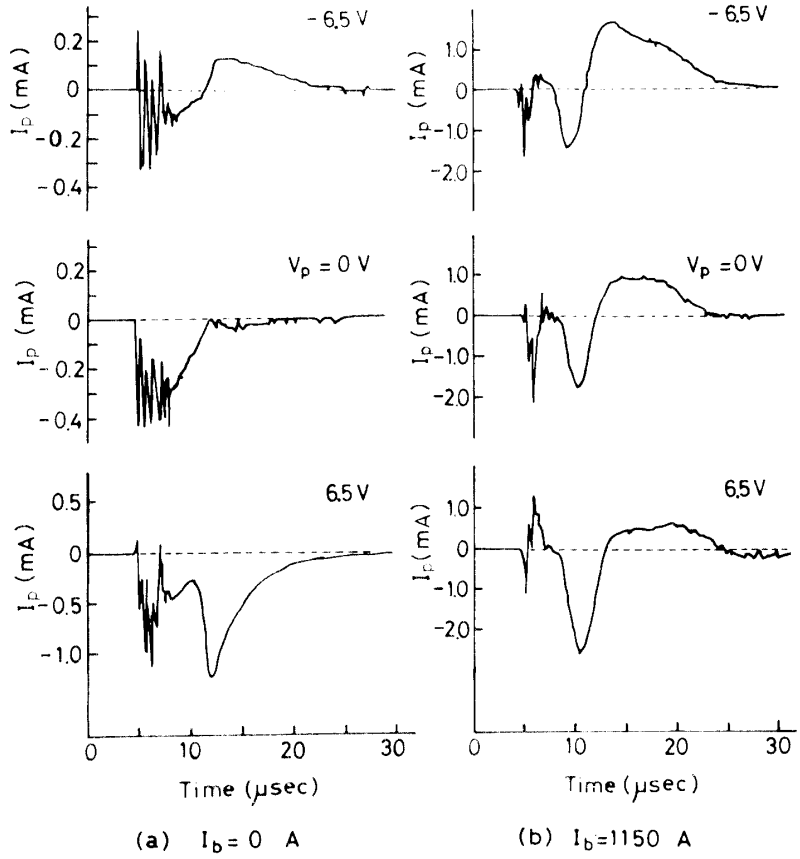

Fig. 27. Probe current measured at the point R = 0 and 22.7 cm by varying the probe voltage V_p.

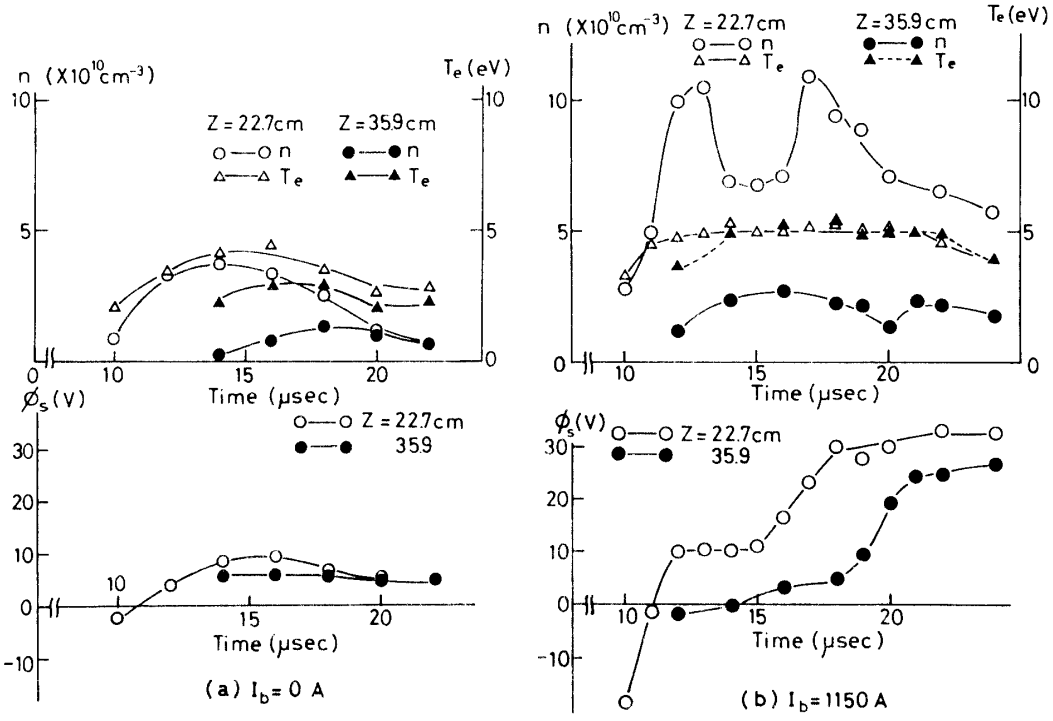

Fig. 28. Time evolution of T_e, n and Φ_S at Z = 22.7 cm and 35.9 cm without(a) and with(b) magnetic field.

The electron temperature T_e is nearly constant value of 5 eV at both positions. The plasma density at Z = 22.7 cm reaches the value of 1.1×10^{11} cm^{-3} which is about two times larger compared with that in Fig. 28(a) and two peaks appear. The first peak seems to be formed by plasma mainly coming into the probe directly and reflected at the magnetic wall in the region of dR/dZ = 0. The second one seems to be due to the plasma which is reflected in the region of the bent coil (i.e. the region of dR/dZ = 0.25) and comes back to the probe again. The plasma potential Φ_S at Z = 22.7 cm shown in Fig. 28(b) is compared with that in Fig. 28(a). The plasma potential Φ_S with magnetic field reaches +10 V at 12 μs and rises again up to +30 V from the time of 16 μs, while the plasma potential Φ_S without magnetic field gradually falls down from 16 μs. The build-up of Φ_S from 16 μs consists with increasing of the plasma which is reflected at the magnetic wall and comes back to the probe. Following this rise of Φ_S at Z = 22.7 cm, the Φ_S at Z = 35.9 cm also rises up. But the inner plasma potential at Z = 22.7 cm is always higher than the outer one at Z = 35.9 cm.

It has been observed in section 5.3.1 that the laser-produced plasma is generated with two groups and expands. It has been reported by Shcurko et al. that the laser-produced plasma which is generated with the aluminum target includes the thermal ions with the velocity of 5–10 eV and the accelerated high energy ions with the velocity of 600 eV. From our experimental results, since the first peak of laser-produced plasma has very fast speed (i.e. high energy) and the second peak has the speed of 2.4×10^6 cm/sec (i.e. 3.5 eV) and propagates relatively slowly, it is considered that the first and the second peaks correspond with the accelerated ions and the thermal ions respectively. As the measured electron temperature of the second peak is about 5 eV from section 5.3.3, it is found that the thermal velocity of this part of plasma is roughly equal to the flow velocity. It needs high magnetic field to confine the plasma with high energy which corresponds with the first peak. It has not been observed the effect of confinement for the first peak in this experiments as mentioned before.

The reason for the generation of plasma potential inside the magnetic wall is considered as follows. The plasma which is produced on the target expands forward and diffuses along the axis Z, being reflected on the magnetic wall. The plasma reaches both ends of the magnetic coil at 15 μs and fills the surmac. After that, electrons escape from the apertures at both ends of the magnetic coil faster than ions due to much lighter mass, and the plasma has positive potential and it increases from +10 V to +30 V. This phenomenon which is a transitional state occurs from t = 15 μs to 18 μs. The potential difference $\Delta \Phi_{sp}$ between the potential at Z = 22.7 cm and that at Z = 35.9 cm using the next equation which shows the ambipolar potential $\Delta \Phi$ [*18*].

$$\Delta \Phi = (kT_e/e) \times \ln(n_1/n_2) \tag{13}$$

Where, n_1 and n_2 are plasma densities at two different points. The potential difference $\Delta \Phi_{sp}$ calculated by substituting the measured plasma densities shown in Fig. 28(b) into the above equation and the $\Delta \Phi_{sp}$ obtained by the measured plasma potential are shown in Fig. 29. In Fig. 29, n_i (= n_1) and n_0 (= n_2) are plasma densities at

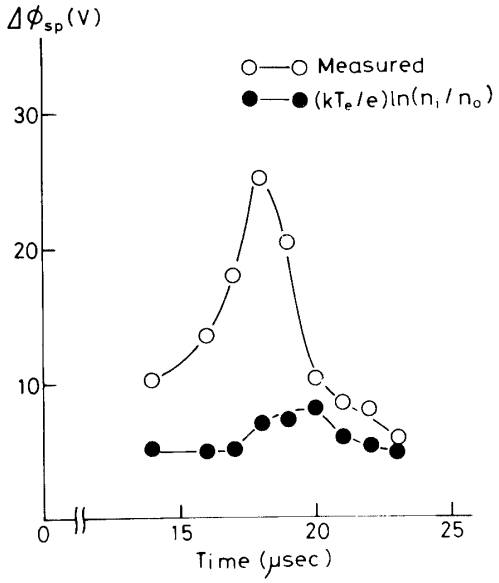

Fig. 29. Potential difference $\Delta\,\Phi_{sp}$ calculated by the measured plasma densities using the equation of the ambipolar (•) and the measured plasma potential (○).

Z = 22.7 cm and 35.9 cm respectively. Although the $\Delta\ \Phi_{sp}$ obtained by the above equation is fairly larger than the $\Delta\ \Phi_{sp}$ obtained by the measured plasma potential between t = 16 μs and 19 μs due to the transitional state of plasma, but they are in good agreement after t = 20 μs.

5.3.4 Effect of plasma confinement on electrical output

The output waveforms of the PDC are shown in Figs. 30(a) and (b) for both cases without and with magnetic field. The peak of the output voltage increases and the duration of the waveform is also longer with the magnetic field. In case of no magnetic field, it seems that a large part of the produced plasma run away to the R-direction and the ions cannot be collected by the ion collector. But, on the contrary, with magnetic field, the plasma is reflected at the magnetic wall and some of them are introduced to the collector. The dependence of magnetic field of the converter output is shown in Fig. 31. The converter output with the magnetic current of $I_b \simeq 1150$ A ($B \simeq 0.08$ T) is about thirty times larger than that of $I_b = 0$.

When the effective diameter of the converter is increased from 4 to 22 cm, the output of the converter of about 2×10^{-4} J ($\simeq 8.2$ W) has been obtained at V_c = 50 V. In this case, the converter is set at 50 cm in front of the target.

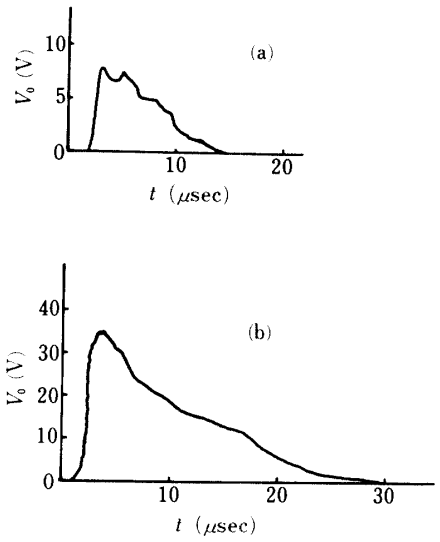

Fig. 30. Output from the PDC as a function of time for without (a) and with (b) magnetic field.

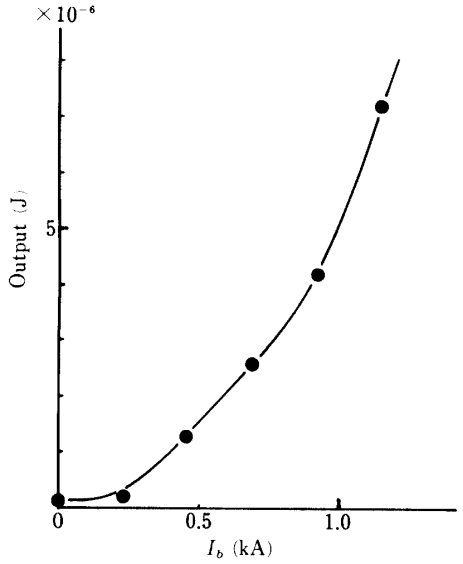

Fig. 31. Dependence of magnetic field of the converter output.

5.4 Conclusions

We have generated laser plasma inside surrounded by the magnetic wall and studied about the characteristics of generated plasma, the effect of confinement and the generation of plasma potential for the fundamental study of the energy conversion from laser beam energy to electricity on the laser energy transmission for a very long distance. The principal results are summarized as follows.

(1) Laser-produced plasma expands forming two groups.

(2) When the magnetic field is applied around laser-produced plasma, the peak value and half-width of ion saturation current become larger due to the plasma reflected at the magnetic wall.

(3) According to the measurements of axial distribution of I_{si}, the effect of confinement by magnetic wall has been confirmed because of the rapid decreasing of I_{si} from the points of no magnetic wall.

(4) After laser-produced plasma fills inside surrounded by surface magnetic wall at about 16 μs, electrons escape from the apertures at both ends of magnetic coil faster than ions. Therefore plasma potential rises from +10 V to +30 V.

(5) The difference of plasma potential between the points inside and outside of the surmac device appears with magnetic field. As the plasma is a transitional state during the rise of plasma potential, the potential difference is not in agreement with the ambipolar potential. But, the former gradually becomes the value of the latter.

(6) The converter output increases up to about thirty times by the surface magnetic confinement with B $\simeq$ 0.08 T compared with no magnetic confinement.

ACKNOWLEDGMENTS

The authors wish to thank the Institute of Plasma Physics, Nagoya University for giving facilities for the image converter camera.

A part of this work was also supported by the Institute of Space and Astronautical Science of Japan.

REFERENCE

[1] K. Horii: *Researches Report of Electrotechnical Laboratory Headquarters,* **36**, 279 (1972) (in Japanese, unpublished).
[2] P. E. Glaser: U.S. Patent 3781 647 (1973), *Proc. IEEE,* **65**, 1162 (1977).
[3] A. D. MacDonald: *Microwave breakdown in gases,* Chap. 8 (1966).
[4] A. Sona: *Laser and their application,* p. 349, Gordon and Breach, New York (1976).
[5] T. Fujioka, A. Noguchi, A. Sano, T. Uchiyama and M. Obara: *Reports of Special Project Research on Energy,* p. 203, November (1983, unpublished).
[6] A. J. Beaulieu: *Appl. Phys. Lett.,* **16**, 504 (1970).
[7] P. E. Dyer, D. J. James and S. A. Ramsden: *J. Phys. E: Sci. Instrum.,* **15**, 1162 (1972).
[8] C. Yamabe, E. Setoyama, M. Yokoyama and C. Yamanaka: *Japan. J. Appl. Phys.,* **14**, 1995 (1975).
[9] M. C. Richardson, A. J. Alcock, K. Leopold and P. Burtyn: *IEEE J. Quantum Electron.* **QE-9**, 236 (1973).
[10] M. C. Richardson, K. Leopold and A. J. Alcock: *IEEE J. Quantum Electron.* **QE-9**, 934 (1973).
[11] W. J. Sarjeant, A. J. Alcock and K. E. Leopold: *IEEE J. Quantum Electron.* **QE-14**, 177 (1978).
[12] R. Dumanchin, M. Michon, J. C. Farcy, G. Boudinet and J. Rocca-Serra: *IEEE J. Quantum Electron.* **QE-8**, 163 (1972).
[13] Y. L. Pan, A. F. Berniiardt and J. R. Simpson: *Rev. Sci. Instrum.,* **43**, 662 (1972).
[14] H. Akiyama, T. Takamatsu, C. Yamabe and K. Horii: *J. Phys. E: Sci. Instrum.,* **17**, 1014 (1984).
[15] T. Y. Chang: *Rev. Sci. Instru.,* **44**, 405 (1973).
[16] M. Yamauchi, H. Homma, T. Nakamura, C. Yamabe and K. Horii: *The Rev. of Laser Engineering,* **15**, 276 (1987, in Japanese).
[17] A. Y. Wong, Y. Nakamura, B. H. Quon, and J. M. Dawson: *Phys. Rev. Lett.,* **35**, 1156 (1975).
[18] S. Kogoshi, H. Asano, M. Kisaka, and T. Sekiguchi: *Jap. J. Appl. Phys.,* **22**, 132 (1983).
[19] Y. C. Lee, T. K. Samec, and B. D. Fried: *Phys. Fluids,* **20**, 815 (1977).
[20] K. Takasugi, H. Akiyama, T. Takai, and S. Takeda: *J. Phys. Soc. Jpn.,* **53**, 193 (1984).
[21] K. Yatsui, S. Miyoshi, H. Takai, K. Shida, K. Ishii, and A. Itakura, *Phys. Rev. Lett.,* **43**, 627 (1979).
[22] V. P. Pastukhov: *Nuclear Fusion,* **14**, 3 (1974).